Biosensors and Bioelectronics 126 (2019) 664–671

Contents lists available at ScienceDirect

Biosensors and Bioelectronics

journal homepage: www.elsevier.com/locate/bios

Ultratrace antibiotic sensing using aptamer/graphene-based field-effect transistors

Xiaoyan Chen[a,b], Ying Liu[a,b], Xian Fang[a,b], Zhuo Li[a,b], Haihui Pu[c], Jingbo Chang[c], Junhong Chen[c], Shun Mao[a,b,*]

[a] *State Key Laboratory of Pollution Control and Resource Reuse, International Joint Research Center for Sustainable Urban Water System, College of Environmental Science and Engineering, Tongji University, 1239 Siping Road, Shanghai 200092, China*

[b] *Shanghai Institute of Pollution Control and Ecological Security, Shanghai 200092, China*

[c] *Department of Mechanical Engineering, University of Wisconsin-Milwaukee, 3200 N. Cramer Street, Milwaukee, WI 53211, USA*

ARTICLE INFO

Keywords:
Antibiotic
Aptamer
Field-effect transistor
Microfluidic chip
Debye length

ABSTRACT

Antibiotic residue, as emerging pollution resulting from antibiotic abuse, poses a serious threat on ecosystem and human health. Conventional methods for antibiotic detection, *e.g.*, liquid/gas chromatography, are based on complicated instruments and time-consuming; therefore, efforts have been made to realize *in situ* and real-time monitoring of antibiotics. Here, a miniaturized and integratable electronic antibiotic sensor based on field-effect transistor (FET) is reported. The reduced graphene oxide (rGO) nanosheet is used as the channel material and the aptamer RNA for tobramycin is modified onto rGO as the probe. A novel sensor design with 6-mercapto-1-hexanol (MCH)/1-pyrenebutanol (PBA) blocking layer (BL) for structure optimization is applied to enhance the sensor reliability and specificity. This rGO/aptamer/BL sensor shows an ultra-sensitivity to tobramycin with a lower detection limit of 0.3 nM and a quick response within 5 s, as well as a high specificity over other antibiotics such as kanamycin, streptomycin, ciprofloxacin, and tetracycline. The sensing mechanism based on the deformation of the charged aptamer probe is proposed *via* an in-depth analysis of the interactions between aptamer, tobramycin and rGO. In addition, sensing test performed under controlled microfluidic flow conditions demonstrates a great potential of the sensors in practical applications.

1. Introduction

Antibiotics have saved countless lives due to their marvelous inhibition to pathogens growth (Fleming, 1929). However, the abuse of antibiotic has caused severe threats to ecosystem and human health. The anxiety from the high concentration of antibiotics in water environment (μg/L level) together with the ever-growing concern on water quality and public health leads to an increasing demand for antibiotic detection in water (Zhang et al., 2015). Conventional antibiotic detection is mainly based on sophisticated instruments, such as liquid chromatography coupled with mass spectrometry (Bayen et al., 2014), gas chromatography (Preu et al., 1998), capillary electrophoresis (Ge et al., 2013), Raman spectroscopy (Li et al., 2013), and ion mobility spectrometry (Li et al., 2012). Though reliable and accurate, they require expensive instrument, trained personnel, and complex pre-treatments. Equipment-free methods such as the microbiological assay and enzyme-linked immunosorbent assay are difficult in providing quantitative analysis and have concerns of enzyme deactivation (Szabó et al., 2017). Currently, there is a great need for simple and rapid antibiotic detection with high sensitivity and specificity. Optical sensors based on fluorescent (Lan et al., 2012), colorimetry (Kim et al., 2010), chemiluminescent (Fang et al., 2018), surface plasmon resonance (Rebe Raz et al., 2009), and electrical sensors based on electrochemistry (Borowiec et al., 2013) have been applied in antibiotic detection and achieved a lower limit of detection (LOD) of nM to μM level. However, since chemical reactions and post-processing are required, these sensors are environmentally unfriendly and are incapable of rapid or real-time detection.

Graphene-based field-effect transistors (GFETs) have been demonstrated as a promising platform for next generation sensors (Mao et al., 2017a). Studies of GFET sensors for gas, water contaminant, biomolecule, and microorganism detection have been reported, showing superiorities in rapid and sensitive detection with a simple and miniaturized structure (Chen et al., 2018b; Mao et al., 2017b). In GFET,

---

* Corresponding author at: State Key Laboratory of Pollution Control and Resource Reuse, International Joint Research Center for Sustainable Urban Water System, College of Environmental Science and Engineering, Tongji University, 1239 Siping Road, Shanghai 200092, China.

E-mail address: shunmao@tongji.edu.cn (S. Mao).

https://doi.org/10.1016/j.bios.2018.11.034
Received 13 September 2018; Received in revised form 19 November 2018; Accepted 19 November 2018

probe functionalization on graphene is the key for sensor selectivity. As for antibiotic molecules with structural complexity, bio-recognizers are useful but are often chemically unstable, *e.g.*, enzyme and antigen/antibody (Kim et al., 2012; Prado et al., 2015). In contrast, a novel bio-recognizer called aptamer has been developed with superiority in stability and specificity through systematic evolution of ligands by exponential enrichment (SELEX) (Itamar and Maya, 2007). Aptamer is an oligonucleotide (RNA/ssDNA) with specific sequence, adaptable to a variety of analytes (*e.g.*, proteins, nucleic acid, and drugs) by forming three-dimensional structures. Sensors using aptamer for selective antibiotic detection have been developed. For instance, chemiluminescence sensors for lincomycin detection were reported based on the competition between aptamer and molecularly imprinted polymer (MIP) (Li et al., 2017), and electrochemical aptamer sensors for aminoglycosides detection were developed based on the antibiotic binding-induced aptamer conformation shift (Schoukroun-Barnes et al., 2014). Thus, aptamer shows advantages, especially high specificity, in antibiotic sensing. However, to the best of our knowledge, GFET with aptamer as the probe for antibiotic detection has rarely been reported (Cheng et al., 2016).

In this study, aptamer RNA was modified onto back-gate GFET as probe for antibiotic detection. Tobramycin (TOB) is a broad-spectrum aminoglycoside antibiotic, which is commonly applied in gram-negative bacillary infections treatment but has a narrow safety margin. The molecular structure of the TOB aptamer as well as its specific interaction with TOB has been maturely studied. The aptamer is capable of folding into a stable "hairpin" structure with tobramycin (Patel et al., 1997). GFET sensors working in aqueous solutions have long been limited by the Debye screening effect since the sensor response is based on the electric effect from the charged target molecule. Thus, on one hand, the target molecule must be charged; on the other hand, the probe to "capture" the target molecule should be close enough to the channel material surface (within Debye length), ensuring that the electric effect works. Distinct from other probes, aptamer itself can induce an electric effect because of the charges along its backbone, which is alterable by transforming the aptamer morphology upon the target molecule binding. Therefore, aptamer may enhance the sensor response, resulting in ultrasensitive GFET sensors used in water. Though applications of aptamer probe in FET sensors have been reported, the influence from the charges of probe has rarely been discussed (An et al., 2013; Farid et al., 2015). Hence, it is of great significance to study the impact of charged probes on GFET sensing response especially when probes transform during the sensing.

In addition to the probe, the reliability issue arising from the nonspecific adsorption of target and interfering molecules becomes a bottleneck for the applications of GFET sensor. Though attempts have been made to shield this effect by depositing a metal oxide passivation layer on the graphene surface (Maity et al., 2017; Thakur et al., 2018), the passivation layer thickness has remarkable effects on sensing performance and the deposition may greatly change the transistor characteristics of graphene. In this study, a novel sensor design with chemical blocking layers modified on sensor surface was carried out by modifying 6-mercapto-1-hexanol (MCH) and 1-pyrenebutanol (PBA) on gold nanoparticles (Au NPs) and reduced graphene oxide (rGO), respectively, through strong chemical interactions (*i.e.*, coordinate bond and π-π stacking). The blocking treatment has effectively eliminated the nonspecific adsorption and improved the reliability and selectivity of the sensor. This blocking strategy offers insights for the design of highly reliable and selective GFET sensors. The novel rGO/aptamer/blocking layer (BL) sensors show rapid (1–5 s) and sensitive response to tobramycin with an LOD of 0.3 nM (0.14 μg/L), and a high selectivity to tobramycin compared with other four antibiotics from three categories. Furthermore, the rGO/aptamer/BL sensors were fabricated with polydimethylsiloxane (PDMS) micro-channels and tested under controlled microfluidic flow conditions, showing inspiring results comparable with those tested in static water.

2. Experimental

2.1. Materials

All chemical reagents used were analytically pure grade and used as received. Tobramycin, kanamycin, streptomycin, ciprofloxacin, tetracycline, 6-mercapto-1-hexanol were purchased from Aladdin Chemical Reagent Co., Ltd. (Shanghai, China), 1-pyrenebutanol was purchased from Sigma-Aldrich Co., Ltd., monolayer graphene oxide was purchased from GaoxiTech Limited (Hangzhou, China). All buffers were prepared with DI water supplied by Milli-Q Ulltrapure Water Purification System (18.4 MΩ cm, Millipore). RNA aptamer probe was synthesized using SELEX, purified by HPLC and functionalized with thiol group, obtained from Sangon Biotech Co., Ltd. (Shanghai, China). The sequences were as follows: thiol-5′-GGCACGAGGUUUAGCUACACUCGUGCC-3′. Antibiotics in forms of tobramycin sulfate, kanamycin sulfate, streptomycin sulfate, ciprofloxacin hydrochloride monohydrate, and tetracycline hydrochloride were prepared with 0.1 mM phosphate buffered saline (PBS) solution.

2.2. Sensor fabrication

Highly-doped silicon wafer with a 300 nm thick surface oxide layer (SiO_2) was used as the substrate with patterned gold interdigitated electrodes. The gold electrodes have finger-width and inter-finger spacing of 2 μm and 1.5 μm, respectively, with a thickness of 50 nm. To bridge the gold finger electrodes, one droplet of 0.001 mg/mL GO aqueous dispersion was pipetted onto gold electrodes. Thermal reduction of GO to rGO was performed in an argon environment under 400 ℃ for one hour. Gold nanoparticles were then deposited onto rGO by vacuum sputter coating using Leica EM ACE 200 sputter coater. The immobilization of aptamer RNA on Au NPs was achieved by incubating the sensing area in an aptamer solution (20 μM) for 12 h. The unbound aptamer residuals were removed by washing the sensor with DI water for several times. To improve the sensor reliability, 6-mercapto-1-hexanol and 1-pyrenebutanol were used to mask Au NPs and rGO through Au-S bond and π-π stacking, respectively.

2.3. Characterizations and static sensing tests

Scanning electron microscope (SEM) was performed on a Hitachi S-4800 UHR FE-SEM. Atomic force microscope (AFM) was performed in contact mode with Nanoscope IIIa Multimode. AFM measurements were performed in air with Au NPs, Au NPs/aptamer, and Au NPs/aptamer/TOB on rGO/SiO_2/Si substrate. The Au NPs/aptamer/TOB sample was prepared by incubating Au NPs/aptamer in TOB solution for an hour and washed with DI water and dried in air. The electrical properties of the sensors and their sensing performance were analyzed using a Keithley 4200-SCS semiconductor system. In the I–V measurement, the drain-source voltage (V_{ds}) was swept from −1.0 V to +1.0 V (0.02 V/step) while the drain-source current (I_{ds}) was recorded. In the transistor measurement, I_{ds} was recorded under a fixed V_{ds} (+0.1 V) while sweeping the gate voltage (V_g) from −40.0 to + 40.0 V (0.05 V/step). The sensing testes were carried out with a V_{ds} of +0.1 V with drop by drop sample solution putting on the sensing area. All electrical measurements were performed in the ambient condition.

2.4. Microfluidic chip and dynamic tests

Microfluidic chips were integrated by PDMS channels with a width of 600 μm and a depth of 200 μm. In dynamic test, the sample solution was driven and controlled by a micro-injection pump (Longer, LSP04-1A) and flow through the channel at a flow rate of 50 μL/min. The sensing tests in microfluidic channels were carried out with the same parameters of those with static water.

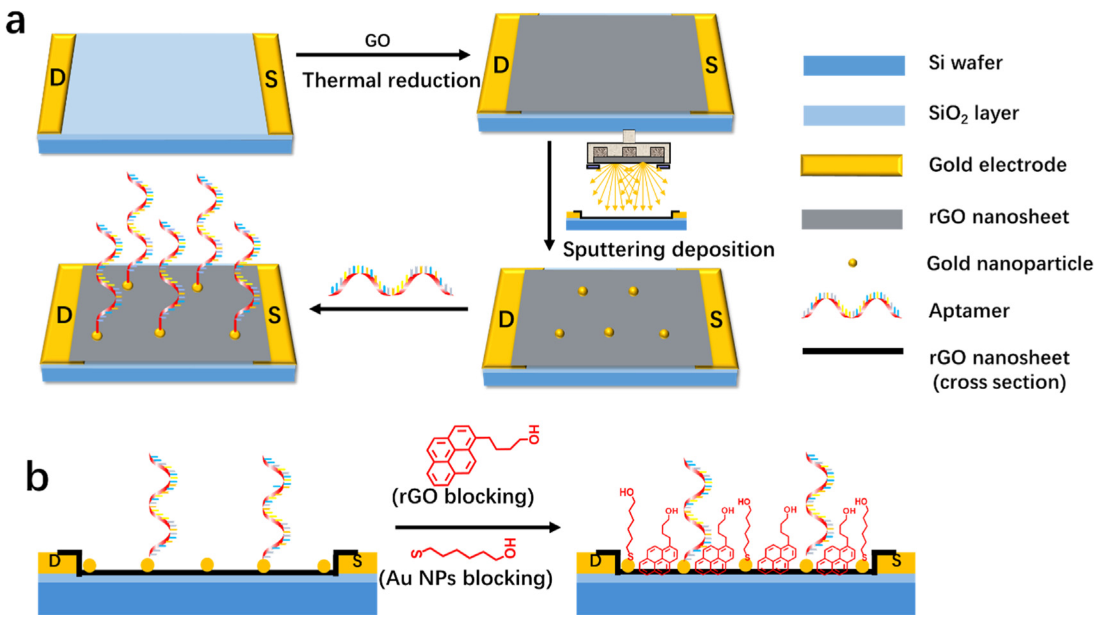

Fig. 1. Schematic diagram of (a) rGO/aptamer FET sensor and (b) chemical blocking steps.

3. Results and discussion

3.1. Device characterizations

The schematics of sensor fabrication and chemical blocking are shown in Fig. 1. In this GFET sensor, rGO works as the sensing channel material and the aptamer is linked to rGO surface through Au NPs. The hybrid rGO/Au NP structure was analyzed based on SEM and TEM. Fig. S2a (Supplementary Material) shows the SEM image in which a single rGO nanosheet spans across two adjacent gold electrodes (*i.e.*, the source and the drain) as the channel material. The Au NPs deposited on rGO have a uniform distribution and high area density, providing binding sites for aptamer modification. The aptamer deformation is important for the understanding of sensing mechanism and can be qualitatively characterized by the altitude variation of the probe; therefore, AFM measurements were performed with Au NPs, Au NPs/aptamer, and Au NPs/aptamer/TOB on rGO/SiO_2/Si substrate. Fig. S2b, d and e show AFM images of Au NPs, Au NPs/aptamer, and Au NPs/aptamer/TOB on the rGO/SiO_2/Si substrate, respectively; while the corresponding height profiles are shown in Fig. S2c, f and g. The bright dots and humps in AFM images represent the Au NPs and Au NPs/aptamer. It shows that Au NPs have a height (size) of 0.6–1.6 nm with an average size of 1.22 nm. The aptamers modified on Au NPs have a height of 3–10 nm and an average height of 6.69 nm. In comparison, after adding TOB, the height values reduce to 2–6 nm with an average height of 4.19 nm, and the overall probe altitude shows an obvious decrease. It was inferred that the aptamer has specific interactions with TOB, resulting in the folding of RNA chain to a stable 3D “hairpin” structure. The deformation of the aptamer upon the TOB interaction leads to a decrease in the height and the aptamer is “closer” to the rGO surface. Based on the AFM results, the aptamer modification and its geometry transformation were identified, which could help understand the sensor response in the TOB sensing.

The electrical characteristics of the rGO and rGO/aptamer FETs are presented in Fig. 2**a-b**. In Fig. 2**a**, the dependence of drain current *vs.* source-drain voltage of the rGO FET obtained by I-V measurement shows linear relation, indicating an Ohmic contact between rGO and electrodes with a small Schottky barrier (Li et al., 2016). After functionalization with aptamer, the I-V curve of GFET remains linear though the dV/dI slope slightly decreases. It suggests that the stable Ohmic behavior is well preserved after the probe modification, and that the aptamer functionalization on rGO has a reliable electrical contact for sensor test. The transfer characteristics are the basis to study the sensing mechanism of FET sensors. The transfer curves (Fig. 2**b**) indicate a p-type semiconducting nature of the GFET plateforms in an ambient environment (hole is dominant in electric conduction), which is typical for thermally-reduced GO (Chen et al., 2016; Yu et al., 2015). After the aptamer modification, the Dirac point (V_D) of the transfer curve shifts from 23.7 V to 34.8 V, indicating the aptamer functionalization leads to an increase in hole carrier density of rGO (*i.e.*, p-type doping). To explain this change, the charge state of apatmer RNA should be taken into account. As shown in Fig. 3**a**, the nucleotide chain in aptamer is linked by phosphodiester linkage (*i.e.*, phosphate backbone), which is negatively charged due to the hydrolysis effect. When aptamer was modified on rGO, the negative charges in phosphate backbone lead to an increase in hole density of rGO *via* electrostatic effect. In addition, the overall decrease in current and the declined slope at p-type conductive region ($Vg < V_D$) are due to the crystal lattice and impurities scattering, both of which resulted from the deposited Au NPs. The current decrease also matches with the slightly decreased dI/dV in I-V measurements. As a consequence, the aptamer/rGO FET shows a p-type characteristic and the channel material has an Ohmic contact with the electrodes, which enables a reliable sensing test for antibiotics.

3.2. Antibiotic detection

The back-gate FET sensors with rGO-based platform were used for TOB detection and the real-time responses were obtained by drop-by-drop addition of the antibiotic solution with different concentrations. Since each sensor device has a different initial resistance due to the difference in rGO distribution, a normalized current (I/I_0) is defined and used as the response for reliable analysis. The response curve of bare rGO FET to TOB (Fig. 2**c**) shows a slightly declined trend, which is due to the adsorption of TOB on rGO surface by hydrophobic interaction. Because of the hydrolysis of amino-groups ($–NH_2 + H_2O \rightleftharpoons –NH_3^+ + OH^-$), TOB molecules are positively charged, and the electrostatic interaction leads to a decrease in hole density of rGO. However, since the hydrophobic interaction force is weak, the sensor response is insignificant and the sensor current does not show a permanent change to TOB. In contrast, after aptamer modification (Fig. 2**d**). the sensor current sharply increased and maintained when antibiotic solutions were added. The response time is determined to be

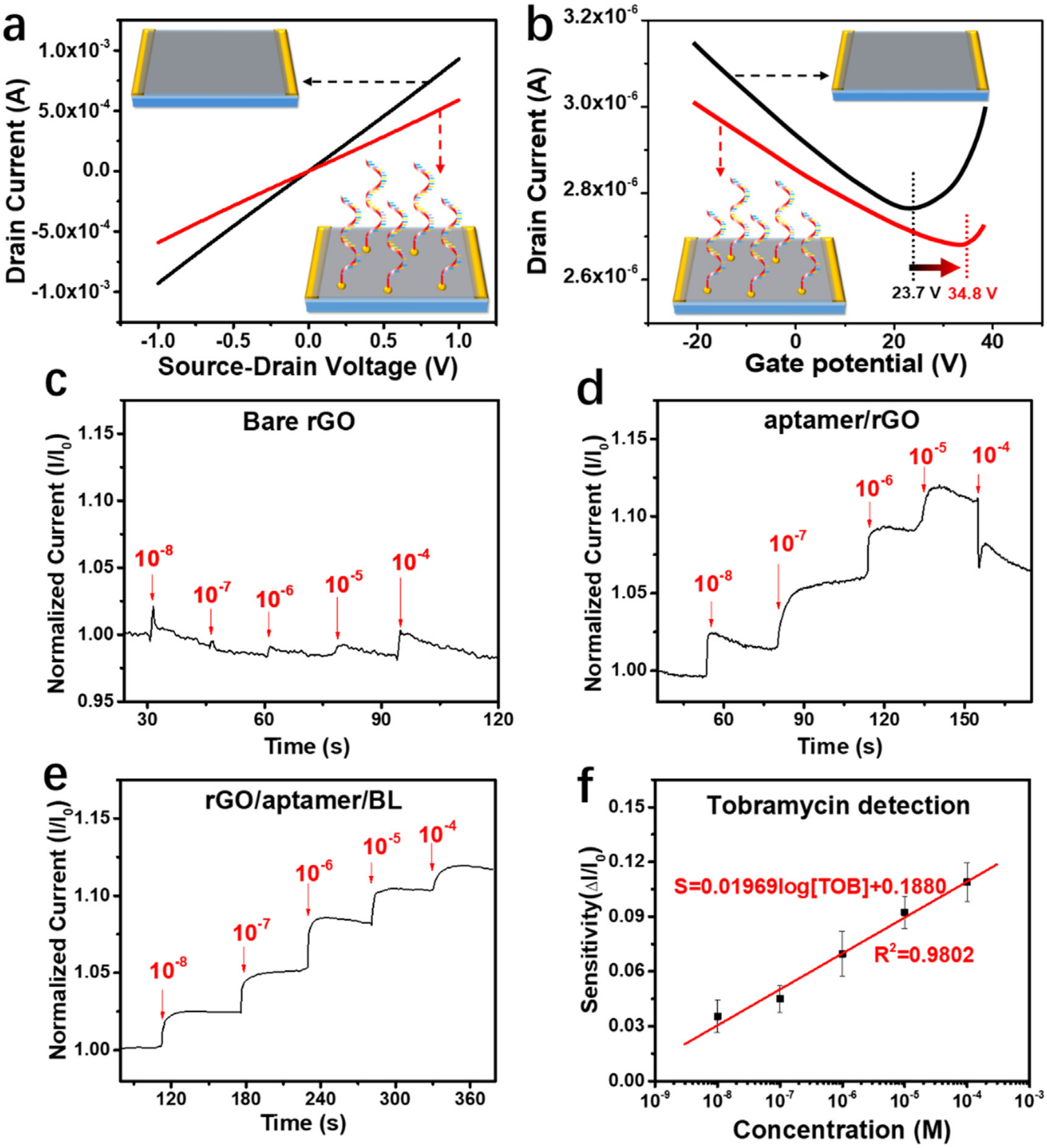

Fig. 2. (a) I-V measurement results before and after aptamer modification on rGO (V_{ds} = −1.0 to +1.0 V). (b) Device transfer characteristics before and after aptamer modification on rGO (V_{ds} = +0.1 V, V_g = −20 to +40 V). Real-time current responses of (c) rGO, (d) rGO/aptamer, and (e) rGO/aptamer/BL sensors to tobramycin. *I* is the response current and I_0 is the initial current in DI water; $\Delta I = I - I_0$. (f) The sensitivity ($\Delta I/I$) *vs.* the tobramycin concentration in the logarithmic coordinate.

1–5 s, which is superior to most of antibiotic detection methods that require minutes or longer to respond (*e.g.*, chromatography and electrochemical sensors). Note that the current increase is not caused by adsorption of TOB on rGO, which actually leads to a current decrease, nor the conductivity of TOB solution itself (the solution conductivity has a negligible effect on sensor response as reported in our previous work (Chen et al., 2018a)).

The aptamer used in this study has specific non-covalent interactions with TOB by forming a “hairpin” structure, as shown in Fig. 3**b** (Jiang et al., 1997; Patel et al., 1997). Specifically, hydrolyzed –NH_2 in TOB electrostatically attract negatively charged phosphate groups in aptamer, while –NH_2 and –OH in TOB bind to bases and phosphate groups in aptamer by hydrogen bonding, respectively, together with the strict complementary nature of the base pairs in aptamer. Since TOB and aptamer are morphologically and chemically complementary, they can form a stable three dimensional “hairpin” structure. It should be noted that the as-prepared aptamer is chemically stable, and the space steric effect prevents specific base pairing in single-stranded RNA until folding with TOB. Since FET sensors are tested in aqueous environment, Debye screening effect should be considered to explain the sensor response. Debye screening is based on electric double layer theory which suggests that a charged ion in solution has electrostatic interaction with other ions around, and the furthest effective action distance is called the Debye length, defined by Eq. (1) (Vacic et al., 2011):

$$\lambda_D = \frac{1}{\sqrt{4\pi l_B \sum_i \rho i z_i^2}}, \qquad (1)$$

where l_B is the Bjerrum length (0.7 nm), ρ_i is the ion density and z_i is the valence. In this study, the Debye length of the sensing environment is 5.88 nm, which is mainly determined by the buffer solution (*i.e.*, 0.1 mM PBS solution). Thus, those charged species located within 5.88 nm from rGO surface are able to electrically influence the channel material. To facilitate understanding, the schematic of the working mechanism is presented in Fig. 3**c**. In principle, the aptamer-TOB

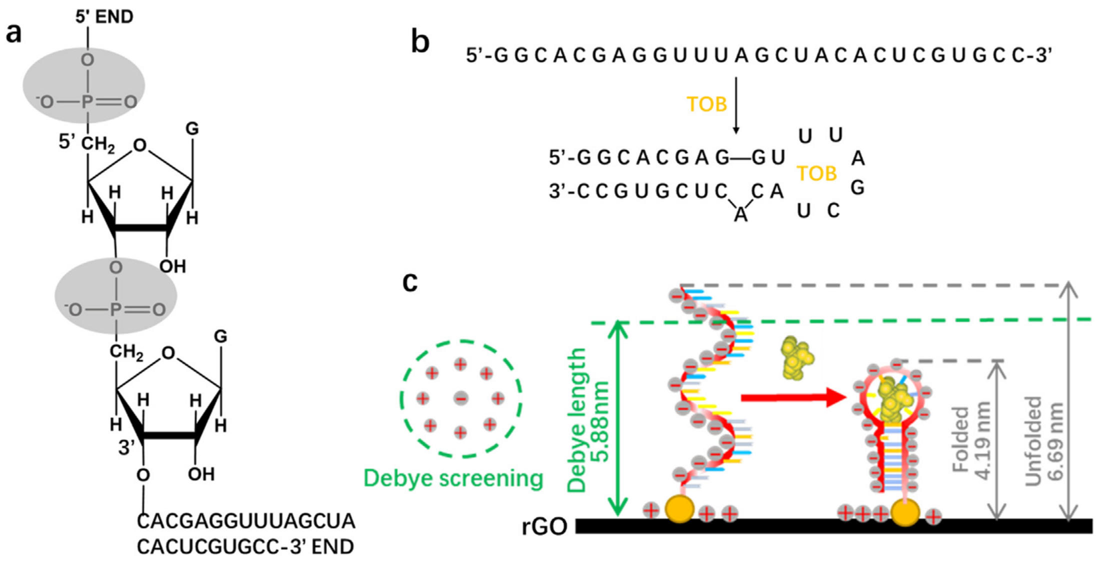

Fig. 3. (a) Structural formula of aptamer; (b) "hairpin" structure formed by aptamer and TOB; (c) the Debye screening effect in sensing environment and the aptamer conformation before and after introducing TOB. The Debye length and average sizes of unfolded and folded aptamers are 5.88 nm, 6.69 nm, and 4.19 nm, respectively.

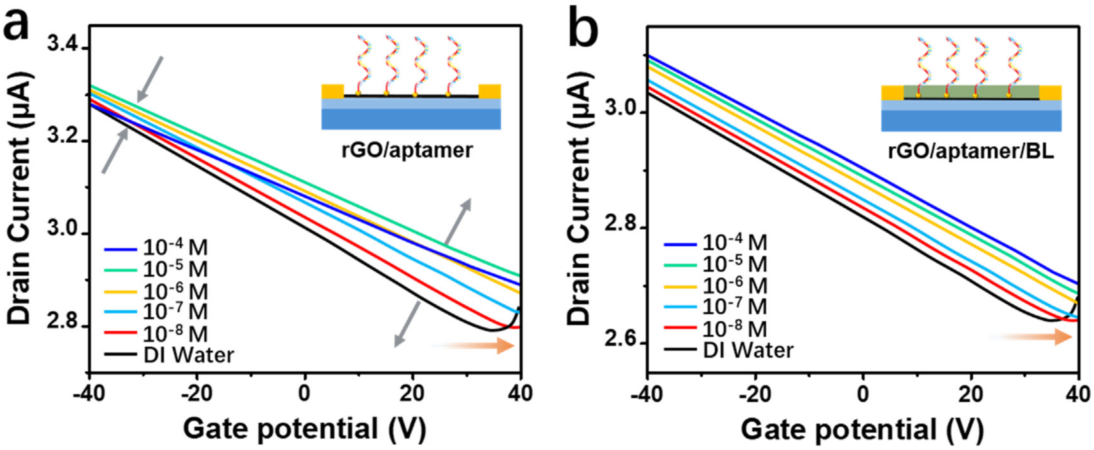

Fig. 4. Transfer curves of (a) rGO/aptamer sensor and (b) rGO/aptamer/BL sensor in TOB solutions at a concentration range from 0 to 10^{-4} M.

complex was formed with the addition of TOB. As a result, by forming the "hairpin" structure, the nucleotides from the 3'-end becomes closer to the rGO surface, which means some of the negatively charged phosphate groups in those nucleotides are within the Debye length (5.88 nm) after the aptamer deformation. Therefore, the structure deformation leads to an increase in the hole density of rGO by the electrostatic effect and the rapid formation of aptamer-TOB complex contributes to the sharp current increase in the dynamic response curve.

Remarkably, for the rGO/aptamer sensor, an obvious current decrease was observed at a high TOB concentration (10^{-4} M). This is due to the direct adsorption of TOB on bare rGO and the impurity scattering effect. At low concentrations (10^{-8}-10^{-5} M), TOB molecules are captured by aptamer first rather than physical adsorption on rGO because of the specific and strong affinity compared with hydrophobic interaction. At a high concentration (10^{-4} M), the aptamer probes are saturated with TOB, then the residual positively-charged TOB molecules accumulate on the rGO surface and lead to a decrease in the hole density. On the other hand, high concentration of antibiotics results in scattering effect on rGO, which may also reduce the carrier mobility.

3.3. *Structure optimization*

The direct adsorption of TOB and ion-induced scattering on bare rGO brings uncertainties in the sensor signal, which hinders the reliable and quantitative sensing. To address the direct adsorption issue, chemical blocking treatment was established. The chemical blocking layer is composed of MCH and PBA, in which MCH bonds to residual bare Au NPs by Au-S bond, while PBA is modified on rGO by π-π stacking. To study the influence of blocking layer on the sensor electrical characteristics, the transistor characteristics of rGO/aptamer FET with the blocking layer are shown in Fig. S3. The transfer curve has a very tiny change after being modified with MCH and PBA, indicating a negligible impact on electronic properties of the rGO/aptamer sensor (Kybert et al., 2014). The dynamic responses of rGO/aptamer/BL sensor to different levels of TOB are shown in Fig. 2**e**. The sensor current rapidly increases with the addition of TOB. Moreover, the current decrease at a high concentration is eliminated and the sensor has a more stable sensing performance (lower background noise and smaller current drift). To better show the effect of blocking layer on the signal improvement, responses of other typical samples are shown in Fig. S4.

To study the significance of blocking layer on the sensing performance, the transistor characteristics of sensors were investigated with TOB of various concentrations (Fig. 4). Carrier density and mobility are two critical factors in determining the conductivity of GFET. The evolution of transfer curves with different TOB concentrations shows the independent variation of carrier density and mobility. The carrier mobility could be described by Eq. (2) (within p-type conducting area) (Chen et al., 2009):

$$\sigma^{-1}(V_g) = [\mu C_g(V_D - V_g)]^{-1} + \sigma_s^{-1}, \tag{2}$$

where μ is the carrier mobility, C_g is the gate capacitance per unit area (11.5 nF/cm^2 for the 300 nm thick SiO$_2$), and σ_s is the saturation conductivity ($V_g \rightarrow +\infty$). In principle, the conductivity can be directly evaluated by current, then Eq. (2) is converted into Eq. (3):(Ping et al., 2016)

$$I^{-1}(V_g) = [e\alpha\mu(V_D - V_g)]^{-1} + I_s^{-1}, \tag{3}$$

where e and α are constants, referred to as electron charge (1.6×10^{-19} C) and correlation coefficient of gate voltage to carrier number density (7.2×10^{16} cm^{-2} V^{-2}), respectively. From which, the relation of the carrier mobility (μ) *versus* I and V_g is obtained as $I/V_g \propto \mu$; that is, the carrier mobility is in proportion to the slope of the transistor curve. Based on the results shown in Fig. 4, the transfer curves of rGO/aptamer sensor show deceased slopes with the increase of TOB concentration. In contrast, GO/aptamer/BL sensor shows a constant slope. This indicates that the carrier mobility of rGO/aptamer decreases during the TOB sensing but maintains at a fixed value in the rGO/aptamer/BL sensor. Since the mobility decrease is attributed to the carrier scattering effect from ions adsorbed on rGO, it suggests that the chemical blocking layer prevents the sensing platform from ion scattering. Moreover, right shifts of Dirac point in both sensors are observed with increased TOB concentration, indicating the increase of hole density in rGO, induced by the aptamer folding. Note that there is a significant change in the transfer curve with 10^{-4} M TOB for the rGO/aptamer sensor, which matches with the dynamic response shown in Fig. 2**d**. As we discussed, with the blocking layer, the dramatic current change at the high concentration is eliminated. The evolution of transfer curves at different TOB concentrations further confirms the proposed sensing mechanism and the effect of blocking layer.

With the blocking layer, quantitative TOB sensing was performed with the rGO/aptamer/BL sensor. Here we define the sensor's sensitivity (S) by $\Delta I/I_0$ ($\Delta I = I\text{-}I_0$). Parallel experiments were carried out on 6–10 similar sensors, and the sensitivity *versus* antibiotic concentration (in log) is plotted in Fig. 2**f**. The data points show a linear correlation of S = 0.01969log[TOB] + 0.1880 (R = 0.9901), where [TOB] is the TOB concentration. The maximum noise level was determined as 0.051% from real-time response curves. With a defined signal-to-noise ratio of 3, the LOD of the rGO/aptamer/BL sensor was determined to be 0.3 nM (0.14 μg/L). This detection limit is below the normal concentration of antibiotics in water at μg/L level and superior to conventional sensors based on electrochemistry (over nM level).

3.4. Selectivity study

Selectivity is a critical index of sensors for practical use. In this study, another four antibiotics from three categories were tested. Kanamycin (KAN) and streptomycin (STR) are another two commonly used aminoglycosides; ciprofloxacin (CIP) and tetracycline (TET) belong to quinolones and tetracyclines, respectively, and both widely exist in water environment. By comparing sensing results of these antibiotics with TOB, the family-selective or individual-selective detection with this sensor is demonstrated. Fig. 5**a** shows the sensor responses to TOB, KAN, STR, CIP and TET at a concentration of 10^{-8}-10^{-4} M. The sensors show no responses to CIP and TET, but with observable responses to KAN and STR when the concentration reaches 10^{-6} M. To compare the sensitivity, the sensitivities of five antibiotics at each concentration are summarized in Fig. 5**b**. The sensor shows a sensitivity of 1.2% and 2.1% to 10^{-5} M KAN and STR, respectively. Although they are above the noise level, they are much smaller than that of TOB (10.3%). Since KAN, STR, and TOB are aminoglycoside antibiotics, they have similar molecular structures as shown in Fig. S1. The aminoglycosides are composed of amino sugar and aminocyclitols by glycosidic linkage, all of which have hydroxyl, amino, cyclohexyl, and pyranyl groups. Thus, the aptamer folding may also happen when introducing KAN and STR. However, the difference of the chemical structures (*i.e.*, function groups distribution) leads to low degree or odds for aptamer folding with KAN or STR. So, the weak interaction only leads to small sensor responses at high concentrations. Selectivity tests with rGO and rGO/aptamer platforms were also carried out for KAN, STR, CIP, and TET (Fig. S5). The results further confirm that the aptamer and blocking layer are needed for specific sensing of TOB.

Since antibiotics often coexist in water, the selectivity was studied with a mixture of antibiotics. As shown in Fig. 5**c**, the sensing test was performed with continuous addition of KAN, STR, CIP, TET, and TOB. The sensor current shows slight increases to KAN and STR, and almost no response to CIP and TET. In contrast, the sensor current shows a significant increase to TOB. The results further confirm the high selectivity of the rGO/aptamer/BL sensor to TOB. Additionally, attempts were made to quantify the influence of coexisting antibiotics to TOB sensing. Four two-component solutions with TOB and one nonspecific antibiotic (both at 10^{-5} M) were prepared. The sensor responses and sensitivities are summarized in Fig. 5**d**. Each of them shows similar sensitivity (10.21%, 10.39%, 9.91%, and 9.99%) to that of the individual TOB solution (10.06%). The results confirm that, even at high concentrations, coexisting antibiotics has limited impact on the TOB signal, which is due to the absolute superiority/specificity of TOB binding with the aptamer rather than other antibiotics. The sensing tests of mixed antibiotic solutions provide further evidence for the extremely high selectivity of rGO/aptamer/BL sensor to TOB.

3.5. Real-time detection on microfluidic chips

In practical applications, especially *in situ* and real-time monitoring, sensors should work in a flowing water condition other than a static state. Since most of the previous studies on GFET sensors were carried out with static solutions, the impacts of water flow on the sensor sensitivity, response time, and stability were not fully understood. In this study, microfluidic chips were integrated with the sensor by attaching PDMS micro-channels onto the sensor substrate. The schematic and optical photograph for the microfluidic chips are shown in Fig. 6**a-b**. During the test, water samples were driven and controlled by an injector pump, which flew into the micro-channels over the sensing area, forming a steady flow environment.

In real-time sensing tests on microfluidic chips, DI water was first injected into the microfluidic channel at a constant flow rate of 50 μL/min, then TOB solution was injected at the same flow rate for a period of time and switched back to DI water at the last stage. As shown in Fig. 6**c**, the sensor current is relatively stable with DI water and increases upon the injection of TOB. It is noticed that during the entire measurement process, there were vibrations at a high but regular frequency in current, which may come from the inherent working frequency of the pump. The maximum vibration amplitude is measured as 1.5%, much higher than the maximum noise under static water (0.051%). Nevertheless, the response signals of TOB at 10^{-4} M, 10^{-6} M, and 10^{-8} M can be distinguished and a higher concentration leads to a higher current increase. Since there is no significant signal when injecting pure buffer without TOB, the current increase can be attributed to the addition of TOB. The sensor sensitivities on microfluidic chips are calculated as 2.5%, 5.5%, and 12% for 10^{-8} M, 10^{-6} M, and 10^{-4} M TOB, respectively, which are comparable with those in the static water. The sensor response time is determined to be 4–7 s, a little longer than that in the static water, which is reasonable considering the flow and static conditions. To better understand the sensor response, experiments were also carried out by injecting the same TOB solution for three times as well as injecting a pure buffer/low concentration TOB after sensing a high concentration TOB (Fig. S6). It shows that only the first injection leads to the current increase and the following injections

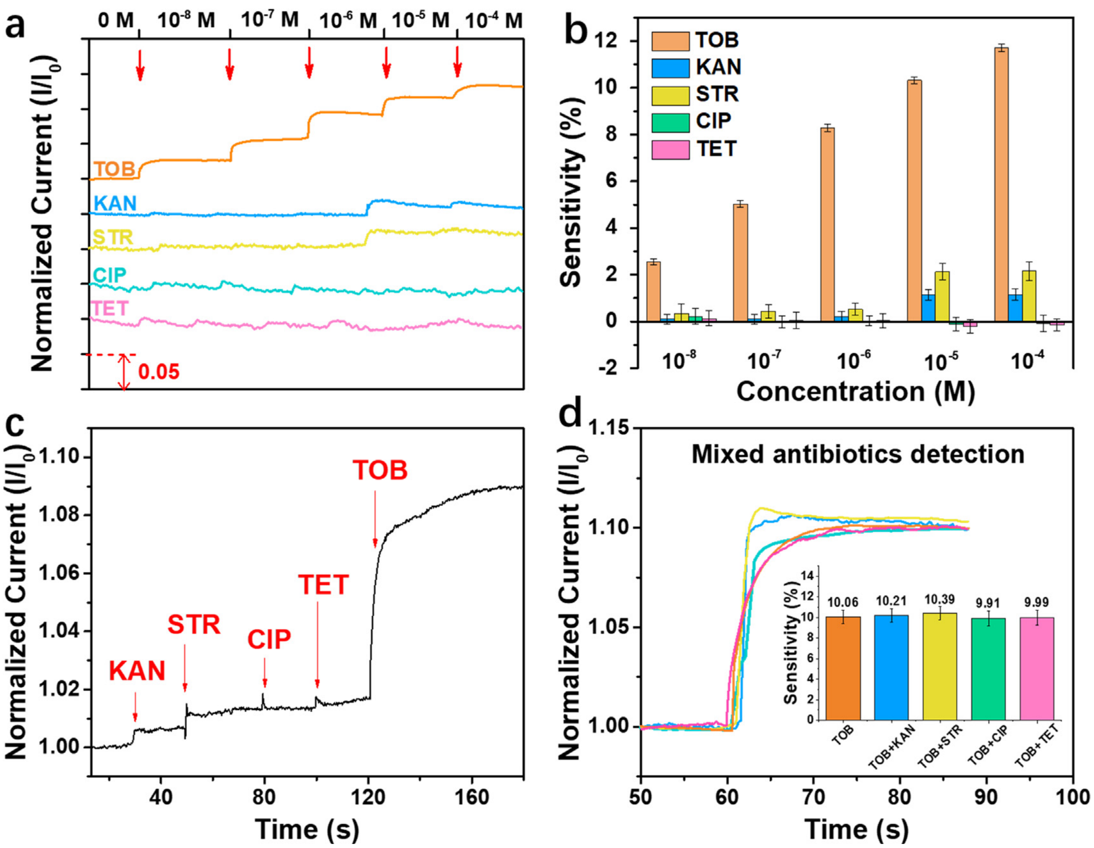

Fig. 5. (a) Real-time responses of rGO/aptamer/BL sensors to various antibiotic solutions: TOB, KAN, STR, CIP, and TET. (b) Summary of the sensitivities at varying concentrations. (c) Real-time responses of rGO/aptamer/BL sensor to KAN, STR, CIP, TET, and TOB at the same concentration (10^{-6} M) in a continuous test. (d) Sensing tests on rGO/aptamer/BL sensors to TOB and mixed antibiotic solutions (both at 10^{-5} M). Error bars are obtained by four sensors for each test.

do not increase the sensor current. In contrast, injection of TOB with a higher concentration (Fig. 2**e**) shows a further current increase. It can be inferred that there is an equilibrium state between the TOB and aptamer. When the sensor current increases and stabilizes after testing with a certain concentration of TOB, only higher concentration of TOB can change the equilibrium state, leading to more binding of TOB with aptamer and current increase. The unrecoverable sensing signal after the reinjection of pure buffer indicates that the sensor is a single use sensor. The unfolding of aptamer RNA and release of antibiotics can be achieved by high temperature treatment; however, the high temperature may disrupt the non-covalent interactions and the sensor structure, *e.g.,* the rGO/Au NP hybrid structure and the integrity of the blocking layers, posing a threat to device properties. Therefore, moderate treatment to selectively unfold the aptamer and unbind the antibiotics and preserve the integrity of the sensor structure is preferred to enable the reuse of the sensor. The specificity of the rGO/aptamer/BL sensor was also characterized on microfluidic chips. The test was performed with sequential injections of KAN, STR, CIP and TET solutions (10^{-6} M), as shown in Fig. 6**d**. There is no notable response to these non-specific antibiotics, confirming the specificity of rGO/aptamer/BL sensors to TOB. The sensing tests on microfluidic chips demonstrate the operation capacity of the sensors in terms of the sensitivity, specificity, and stability. The promising performance under controlled microfluidic flow conditions suggests a great potential of the sensors for practical applications in antibiotic monitoring in water.

4. Conclusions

We have developed a label-free antibiotic sensor based on GFET devices with rGO as the channel material, aptamer RNA as the probe, and MCH/PBA blocking layers to improve the sensing reliability. This rGO/aptamer/BL sensor is highly sensitive to tobramycin in aqueous solutions with an LOD down to 0.3 nM and a remarkable response time within 5 s, as well as a high selectivity over other antibiotics from the specific interaction between tobramycin and the aptamer. A novel sensing mechanism on this GFET platform is proposed. The sensing signal is from the deformation of charged probes (aptamer) instead of the simple introduction of charged target molecules on the channel material surface. In addition, real-time detection of tobramycin with microfluidic chips has been achieved, demonstrating the working capability of this sensor in flowing water and its potential for practical applications in real water conditions. This sensor provides a reliable and practical method for real-time and ultratrace detection of antibiotics in water, as well as new knowledge in sensing mechanism of aptamer-based FET sensors. With special sequence design in aptamer RNA or DNA probe, the sensor platform could be used for other antibiotic sensing to achieve high selectivity, which is the one of the challenges for real applications of antibiotic sensors. The use of blocking layers to block the unfunctionalized sensing area can improve the sensor reliability, which is also applicable to other FET sensor designs and applications. It is believed that this study can inspire FET sensor research and development for real-time trace level chemical and biological sensing.

Acknowledgements

This work was supported by the National Natural Science Foundation of China (No. 21707102) and the 1000 Talents Plan of China.

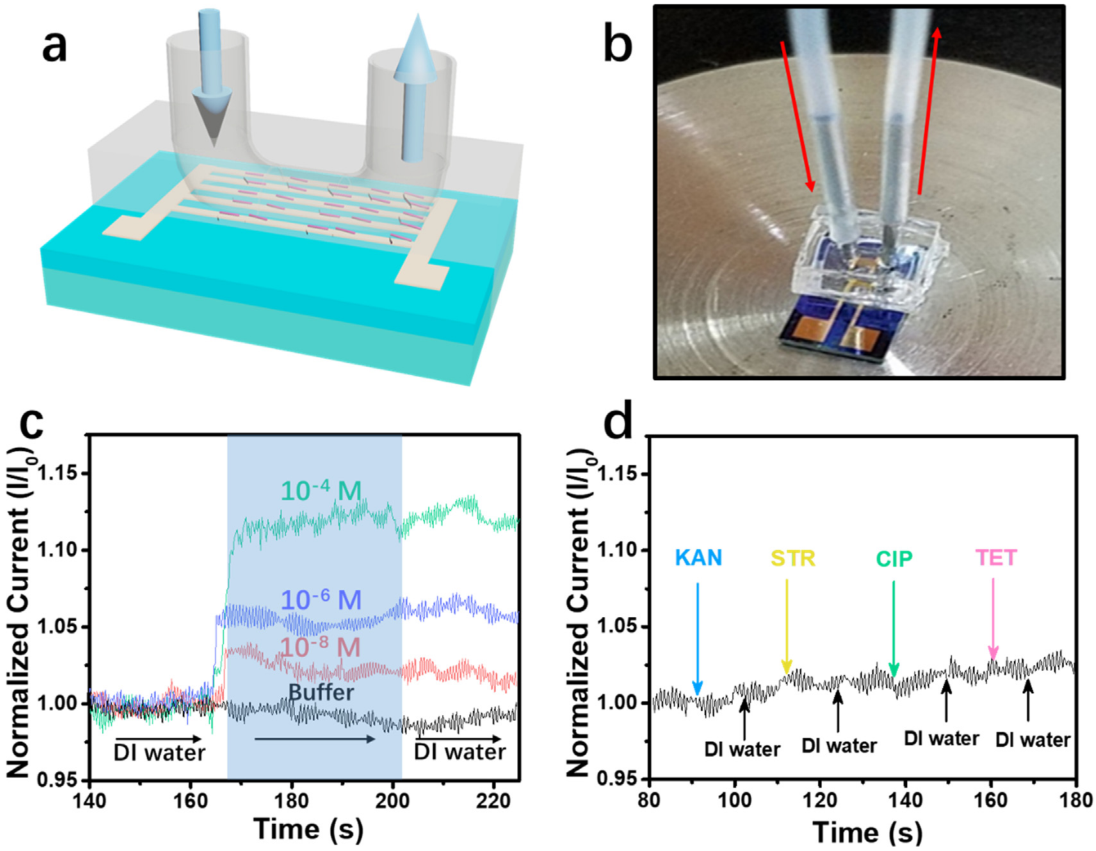

Fig. 6. Real-time sensing tests on microfluidic chips: (a) schematic and (b) optical photographs of the integrated sensor with microfluidic chip. (c) Real-time sensing data by flowing a buffer solution without and with TOB (10^{-4} M, 10^{-6} M, and 10^{-8} M). (d) Real-time sensing data by flowing buffer solutions containing other antibiotics with a concentration of 10^{-6} M.

Appendix A. Supplementary material

Supplementary data associated with this article can be found in the online version at: http://dx.doi.org/10.1016/j.cej.xxxxxx. The antibiotic molecular structural formulas, SEM and AFM results, the transfer curves before and after chemical blocking, other typical sensor responses to tobramycin, the rGO and rGO/aptamer sensor responses to nonspecific antibiotics, control experiments with the microfluidic chip.

Appendix A. Supporting information

Supplementary data associated with this article can be found in the online version at doi:10.1016/j.bios.2018.11.034.

References

An, J.H., Park, S.J., Kwon, O.S., Bae, J., Jang, J., 2013. ACS Nano 7 (12), 10563–10571.
Bayen, S., Yi, X., Segovia, E., Zhou, Z., Kelly, B.C., 2014. J. Chromatogr. A 1338, 38–43.
Borowiec, J., Wang, R., Zhu, L., Zhang, J., 2013. Electrochim. Acta 99, 138–144.
Chen, F., Xia, J., Ferry, D.K., Tao, N., 2009. Nano Lett. 9 (7), 2571–2574.
Chen, H., Chen, P., Huang, J., Selegard, R., Platt, M., Palaniappan, A., Aili, D., Tok, A.I.Y., Liedberg, B., 2016. Anal. Chem. 88 (6), 2994–2998.
Chen, X., Pu, H., Fu, Z., Sui, X., Chang, J., Chen, J., Mao, S., 2018a. Environ. Sci.-Nano 5 (8), 1990–1999.
Chen, X., Zhou, G., Mao, S., Chen, J., 2018b. Environ. Sci.-Nano 5 (4), 837–862.
Cheng, W., Yijun, L., Yibo, Z., Xiaohong, Z., Qiao, L., Miao, H., 2016. Adv. Funct. Mater. 26 (42), 7668–7678.
Fang, X., Zong, B., Mao, S., 2018. Nano-Micro Lett. 10 (4), 64.
Farid, S., Meshik, X., Choi, M., Mukherjee, S., Lan, Y., Parikh, D., Poduri, S., Baterdene, U., Huang, C.-E., Wang, Y.Y., Burke, P., Dutta, M., Stroscio, M.A., 2015. Biosens. Bioelectron. 71, 294–299.
Fleming, A., 1929. Br. J. Exp. Pathol. 10, 226–236.
Ge, S., Tang, W., Han, R., Zhu, Y., Wang, Q., He, P., Fang, Y., 2013. J. Chromatogr. A 1295, 128–135.
Itamar, W., Maya, Z., 2007. Angew. Chem. Int. Ed. 46 (34), 6408–6418.
Jiang, L., Suri, A.K., Fiala, R., Patel, D.J., 1997. Chem. Biol. 4 (1), 35–50.
Kim, B., Lim, D., Jin, H.J., Lee, H.Y., Namgung, S., Ko, Y., Park, S.B., Hong, S., 2012. Sens. Actuator B-Chem. 166–167, 193–199.
Kim, Y.S., Kim, J.H., Kim, I.A., Lee, S.J., Jurng, J., Gu, M.B., 2010. Biosens. Bioelectron. 26 (4), 1644–1649.
Kybert, N.J., Han, G.H., Lerner, M.B., Dattoli, E.N., Esfandiar, A., Johnson, A.T.C., 2014. Nano Res. 7 (1), 95–103.
Lan, M., Liu, W., Ge, J., Wu, J., Wang, H., Zhang, W., Bi, Y., Wang, P., 2012. Chem. Commun. 48 (54), 6818–6820.
Li, Q., Liu, W., Cao, G., Li, X., Wang, X., 2016. Appl. Phys. Lett. 108 (22), 221604.
Li, S., Jia, J., Gao, X., He, X., Li, J., 2012. Anal. Chim. Acta 720, 97–103.
Li, S., Liu, C., Yin, G., Zhang, Q., Luo, J., Wu, N., 2017. Biosens. Bioelectron. 91, 687–691.
Li, Y.-T., Qu, L.-L., Li, D.-W., Song, Q.-X., Fathi, F., Long, Y.-T., 2013. Biosens. Bioelectron. 43, 94–100.
Maity, A., Sui, X., Tarman, C.R., Pu, H., Chang, J., Zhou, G., Ren, R., Mao, S., Chen, J., 2017. ACS Sens. 2 (11), 1653–1661.
Mao, S., Chang, J., Pu, H., Lu, G., He, Q., Zhang, H., Chen, J., 2017a. Chem. Soc. Rev. 46 (22), 6872–6904.
Mao, S., Pu, H., Chang, J., Sui, X., Zhou, G., Ren, R., Chen, Y., Chen, J., 2017b. Environ. Sci. Nano 4 (4), 856–863.
Patel, D.J., Suri, A.K., Jiang, F., Jiang, L., Fan, P., Kumar, R.A., Nonin, S., 1997. J. Mol. Biol. 272 (5), 645–664.
Ping, J., Vishnubhotla, R., Vrudhula, A., Johnson, A.T.C., 2016. ACS Nano 10 (9), 8700–8704.
Prado, T.Md, Foguel, M.V., Gonçalves, L.M., Sotomayor, Md.P.T., 2015. Sens. Actuator B-Chem. 210, 254–258.
Preu, M., Guyot, D., Petz, M., 1998. J. Chromatogr. A 818 (1), 95–108.
Rebe Raz, S., Bremer, M.G.E.G., Haasnoot, W., Norde, W., 2009. Anal. Chem. 81 (18), 7743–7749.
Schoukroun-Barnes, L.R., Wagan, S., White, R.J., 2014. Anal. Chem. 86 (2), 1131–1137.
Szabó, L., Steinhardt, M., Homlok, R., Kovács, K., Illés, E., Kiskó, G., Belák, Á., Mohácsi-Farkas, C., Takács, E., Wojnárovits, L., 2017. Environ. Sci. Technol. Lett. 4 (6), 251–255.
Thakur, B., Zhou, G., Chang, J., Pu, H., Jin, B., Sui, X., Yuan, X., Yang, C., Magruder, M., Chen, J., 2018. Biosens. Bioelectron. 110, 16–22.
Vacic, A., Criscione, J.M., Rajan, N.K., Stern, E., Fahmy, T.M., Reed, M.A., 2011. J. Am. Chem. Soc. 133 (35), 13886–13889.
Yu, C., Chang, X., Liu, J., Ding, L., Peng, J., Fang, Y., 2015. ACS Appl. Mater. Inter. 7 (20), 10718–10726.
Zhang, Q.-Q., Ying, G.-G., Pan, C.-G., Liu, Y.-S., Zhao, J.-L., 2015. Environ. Sci. Technol. 49 (11), 6772–6782.